JSCE | Taylor & Francis
Taylor & Francis Group

RESEARCH ARTICLE

• OPEN ACCESS | Check for updates

The wavedrifter: a low-cost IMU-based Lagrangian drifter to observe steepening and overturning of surface gravity waves and the transition to turbulence

F. Feddersen [a], Andre Amador[a], Kanoa Pick[a], A. Vizuet, Kaden Quinn[a], Eric Wolfinger[b], J. H. MacMahan[c] and Adam Fincham[d]

[a]Scripps Institution of Oceanography, UC San Diego, La Jolla CA, USA; [b]www.Ericwolfinger.com, La Jolla CA, USA; [c]Naval Postgraduate School; [d]Kelly Slater Wave Company and University of Southern California

ABSTRACT

Waves and wave breaking are important to many deep and shallow water processes. We describe the *wavedrifter*, an in situ water-following inertial measurement unit (IMU)-based drifter that measures wave steepening and overturning kinematics, and the subsequent transition to turbulence. The wavedrifter has 5 cm diameter, 77 g mass, and 0.84 saltwater specific gravity. GPS provides time synchronization. MATLAB's Attitude, Heading, Reference System (AHRS) library provides wavedrifter orientation. Laboratory experiments quantify the wavedrifter vertical oscillation mode, water following properties, and ability to reproduce wave spectra for small, $f = 1.5$ Hz waves. The wavedrifter observed wave overturning and the transition to turbulence at the *Surf Ranch* wave basin. Synchronized video observations provide context. The upper-back of the overturn had large ($\approx 4g$) accelerations and $14g$ acceleration magnitude occurs with the impact of the overturning jet. Trajectories reveal the Lagrangian structure of the overturn and subsurface vortex. Although it has limitations, the wavedrifter is a powerful in situ tool to probe wave processes.

1. Introduction

Waves and wave breaking are important to many deep and shallow water processes. Deep water wave breaking drives many aspects of air-sea exchange (e.g. Deike 2022). Shallow water surface wave breaking generates turbulence (e.g. Feddersen 2012), drives nearshore currents (e.g. Feddersen et al. 1998; Haines and Sallenger 1994), and suspends and transports sediment (e.g. Hoefel and Elgar 2003; Vittori 2003). Knowledge of surfzone wave processes is also essential for the estimation of wave runup (e.g. Fiedler et al. 2021) and wave impact forces (e.g. Bullock et al. 2007).

The fluid dynamics of deep and shallow water wave breaking has been examined through both laboratory experimental (e.g. Blenkinsopp and Chaplin 2008; Govender, Mukaro, and Mocke 2023; Lenain, Pizzo, and Melville 2019) and numerical (e.g. Landrini et al. 2007; Derakhti et al. 2020; Mostert, Popinet, and; Deike 2022) studies. Field studies of deep and shallow water waves have leveraged advancements in remote sensing techniques such as optical (e.g. Holman and Haller 2013; Saez, Catalan, and Valle 2021), LiDAR (e.g. Feddersen et al. 2023; Lenain and Pizzo 2020; O'Dea, Brodie, and Elgar 2021), and thermal infrared cameras (e.g. Carini et al. 2015; Jessup et al. 1997). However, remote sensing has its limits, and the detailed fluid

dynamics of wave steepening, overturning, and transition to turbulence remain poorly understood. Thus, there is compelling interest in an in situ instrument that can observe the steepening and overturning of surface gravity waves as well as the subsequent transition to turbulence. Here we present the *wavedrifter* a highly compact, water-following, and low-cost IMU-based drifter that can observe these aspects of surface gravity waves.

Wave buoys (e.g. Longuet-Higgins, Cartwright, and Smith 1963; Mitsuyasu et al. 1975, and many others) estimate second-order wave parameters such as spectra and directional moments, and related parameters such as peak period or significant wave height H_S. The emergence of new technological alternatives for in situ wave observation has facilitated the proliferation of smaller, low-cost, and low-power sensor packages. Following the pioneering work of Herbers et al. (2012), GPS-based wave buoys have proved highly effective in capturing wave spectra and directional moments in the sea-swell ($0.05 < f < 0.3$ Hz) frequency-band (e.g. Amador, Merrifield, and Terrill 2023; Centurioni et al. 2017; Collins et al. 2023; Raghukumar et al. 2019). Wave buoys have also been equipped with inertial measurement units (IMUs; a combination of accelerometers, gyroscopes, and magnetometers).

CONTACT F. Feddersen ✉ ffeddersen@ucsd.edu

Fixed IMUs deployed on ice were initially used to measure surface gravity waves (Kohout et al. 2015; Rabault et al. 2016). Wave-buoy IMU-based systems have since been developed and shown to be accurate in estimating in situ ocean wave spectra at frequencies $f > 0.1$ Hz (Rabault et al. 2022) and $f > 0.25$ Hz (Kodaira et al. 2022). Using a microSWIFT (IMU-based) drifting wave buoy and combining filtering and integrating vertical acceleration for position, buoy and ADCP-based wave heights calculated using a zero-crossing algorithm were consistent in ≈ 4.5 m water depth (Rainville et al. 2023). These GPS and IMU wave buoys are designed only to estimate second-order wave properties such as spectra (or wave height and peak/mean period) and directional moments. However, modern wave buoys have telemetry (e.g. Centurioni et al. 2019; Smit et al. 2021) and are designed to be robust and low power enabling long-duration missions in sea-ice (e.g. Nose et al. 2023) or hurricanes (e.g. Thomson et al. 2023). Identifying wave breaking events also is of interest and a task well suited to IMU-based systems. Accelerations measured by an IMU onboard a 2.15-m long and ≈ 20 kg SWIFT drifter (Thomson 2012; Thomson et al. 2019) were used to classify deep water wave breaking events (Brown et al. 2018). Similar techniques were employed to identify and classify depth-limited breaking events and bore encounters using a 40 cm diameter and 1 kg spherical buoy (Brown and Paasch 2021). Although these IMU-based systems were successful in estimating wave breaking, these systems cannot be considered Lagrangian or water-following in the context of steep, overturning, or broken waves (bores).

An alternative approach that is water-following (truly Lagrangian) is required to study the steeping and overturning of highly nonlinear surface gravity waves and the subsequently generated turbulence. Such a water-following drifter must be small relative to the scales of flow variation within an overturn and be low-mass with relatively high drag. Amador et al. (2012) and Amador and Canals (2016) developed small quasi-Lagrangian IMU-based spherical drifters with 7–10 cm diameters and specific gravity of ≈ 0.8 to measure accelerations within steep, overturning waves. Initial field observations in 2 m plunging waves over a coral reef revealed wave kinematics in an overturn and the subsequent turbulence. Maximum acceleration magnitudes of $20g$ were reported. However, the water-following nature of the drifter was uncertain. Furthermore, there was no synchronization to other instruments or video, and thus the precise part of the wave being sampled was unclear. The use of such quasi-Lagrangian drifters to study wave phenomena has remained largely exploratory and qualitative in nature.

Here, we present the *wavedrifter*, a new water-following (Lagrangian), IMU-based drifter, surpassing its predecessor (Amador and Canals 2016) in terms of compactness, water-following properties, technological sophistication, cost, and versatility. The wavedrifter is described in Section 2. Wavedrifter laboratory and field tests quantify its buoyancy oscillation mode, its response to laboratory high-frequency ($f = 1.5$ Hz) waves, and its water following properties (Section 3). The capability of a wave drifter to observe the kinematics of wave overturning is presented in Section 4 with experiments at the Kelly Slater Wave Company's *Surf Ranch*, a wave basin designed for surfing but used here as a large-scale laboratory. Wavedrifter limitations and improvements are discussed in Section 5. Section 6 provides a discussion and concept for a future experiment.

2. Wavedrifter description

2.1. Exterior housing

The wavedrifter was designed to be water following by co-optimizing two factors : (1) be as small as possible while still containing the electronics and (2) have elevated drag. The exterior housing consists of two half-spheres that when joined form the wavedrifter body, which has an outer-diameter of 5 cm and an inner diameter of 4.18 cm (Figure 1a). Attached to the outer surface of the sphere, three 1-cm wide rings run along the sphere at a latitude of zero degrees (i.e. equator) and longitude of −90, 0, 90, and 180 degrees (Figure 1a). These rings provide extra drag to increase the wavedrifter's water following properties. On the joining surface of the two half-spheres is a groove for an O31 o-ring. The two halves of the wavedrifter exterior housing are joined and sealed using four M2.5 screw/hex nut pairs at four reinforced locations where the rings intersect (Figure 1a,b). A 1.7 cm wide circular port is placed on the exterior housing where an IP68 push-button switch is seated (Figure 1a,b). The two half-spheres were 3D printed with FormLabs Durable resin to ensure strength under pressure and a smooth surface for the O-ring. One side of the external housing is red to be highly visible and the other side is translucent allowing the internal LED to be visible (Figure 1b). The exterior housing with switch was hydrostatically tested to a depth of 7 m without leaking. Exterior housing costs are approximately $150 per wavedrifter.

2.2. Electronics and internal housing

The wavedrifter electronics are enclosed inside the drifter body (Figure 1c,d). The wavedrifter microcontroller is a PJRC Teensy 3.2. A Pololu breakout board for a microSD card is used for data storage. The electronics
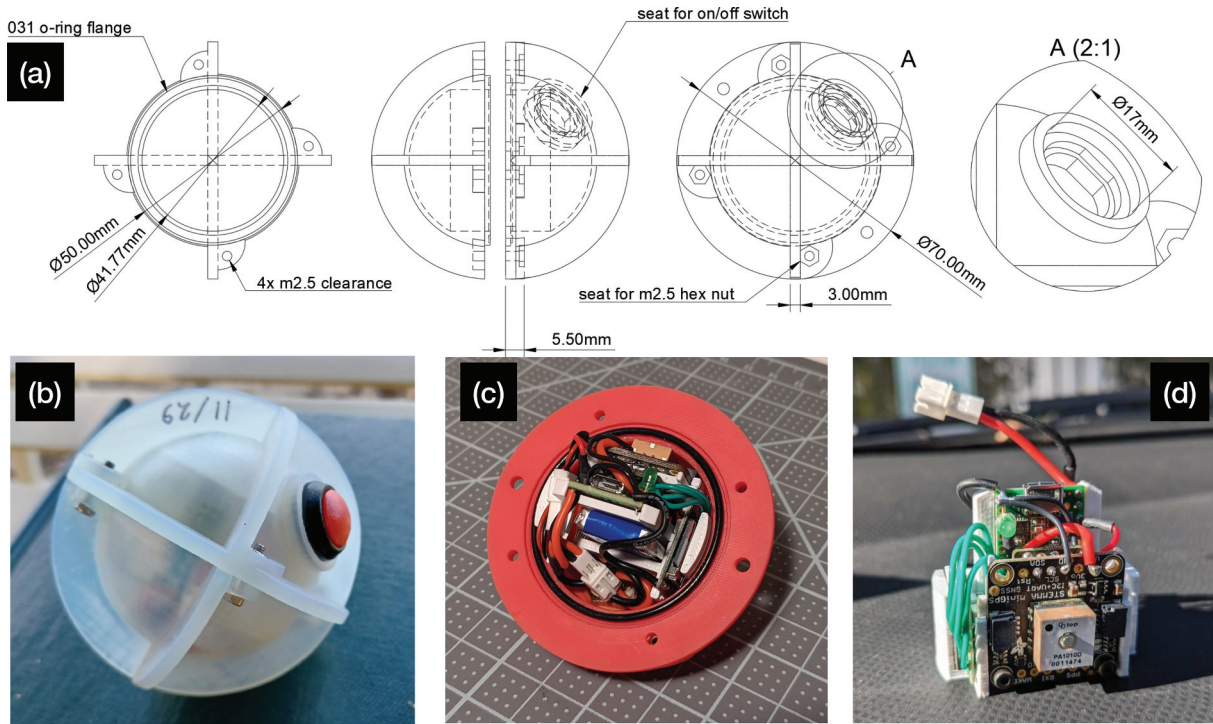
Figure 1. (a) Engineering diagrams of the wavedrifter external housing. (b) Photo of the transparent side of the wavedrifter with switch. (c) Photo of the opened wavedrifter showing the electronics package seated in the external housing and the O-ring. (d) Photo of the electronics package.

are powered by a 3.7 V 250mAh lithium-ion battery. We use the ICM 20,948 9 degrees-of-freedom Micro-electromechanical (MEM) inertial measurement unit (IMU) with accelerometer, gyroscope, and magnetometer that is manufactured by TDK. The IMU is mounted on a breakout board assembled by Pimoroni. The IMU has a $\pm16g$ three-axis accelerometer, a ±2000 dps (degrees per second) three-axis gyroscope, and a three-axis magnetometer with wide range up to $\pm4900\mu T$. IMU acceleration and gyroscope natively sample at 1125 Hz, and their data are low-pass filtered on the board with an 11.5 Hz cutoff frequency. The magnetometer was set to sample continuously at 25 Hz. The IMU data were stored at 25 Hz to include the cutoff frequency within the Nyquist frequency of $f_N = 12.5$ Hz. The Adafruit Mini GPS PA1010D is used as a GPS receiver which provides GNNS strings at 1 Hz with time, latitude, and longitude but no vertical position. Valid GNNS string return was at times intermittent due to wavedrifter submergence. GPS is used here only to provide UTC time to the IMU measurements, allowing for synchronization to other observations such as video. Only a single GPS lock is required for synchronization. The boards for the microcontroller, SD card, IMU, and GPS are attached to PLA 3D printed modules using M2 screw/nut pairs. These modules then snap together forming a single body with an additional groove for the battery (Figure 1b,c). JST connectors run to the external IP68 switch allowing the wavedrifter to be turned on and off. A LED inside the wavedrifter indicates whether the electronics are on or off.

A second LED indicates whether the wavedrifter has acquired a valid GPS-string. Data are written to an ASCII file with time referenced to when the wavedrifter was turned on. Each time the wavedrifter is turned on, a new file with a sequential filename is written. Once GPS lock occurs, IMU sampling time is referenced to GPS time. Battery life is just over an hour. Electronic and internal housing supplies are about $165 per wavedrifter. This cost does not include assembly and wiring costs.

2.3. Wavedrifter mass and buoyancy

The instrumented wavedrifter has a mass of 77.5 g. In saltwater from the Scripps Institution of Oceanography (SIO) pier $\rho \approx 1025$ kgm^{-3}, the wavedrifter reaches neutral buoyancy at a mass of 92.5 g. Thus, the wavedrifter specific gravity in salt water is 0.84 corresponding to a density of 856 kgm^{-3}. In freshwater with $\rho = 1000$ kgm^{-3}, the wavedrifter specific gravity is 0.86.

2.4. IMU noise levels and converting acceleration to earth coordinates

Tests were performed to determine the noise properties of the ICM20948 IMU. A holder for the wavedrifter was fabricated that orients one wavedrifter axis vertically and the others horizontally. There are 24 unique orientations. Wavedrifters were placed in each orientation and held still for 2 min at a time. The resulting data were used to calibrate the accelerometer and diagnose

the IMU noise levels. The accelerometer offset was very small to the point of being negligible. Once calibrated, the IMU accelerometer noise standard deviation is $\sigma_a = 0.0088$ ms^{-2} for each component. Interpreted as white noise, this suggests a spectral noise floor of $\sigma_a^2/f_N = 6 \times 10^{-6}(\text{m}^2\text{s}^{-3})/\text{Hz}$, consistent with the manual quoted spectral noise floor of $5 \times 10^{-6}(\text{m}^2\text{s}^{-3})/\text{Hz}$ (TDK 2017). The gyroscope provides data in rad s^{-1}. For each component, the gyroscope noise standard deviation is 8.3×10^{-4} rads^{-1}, consistent with the manual inferred gyroscope noise of 9×10^{-4}rads^{-1} (TDK 2017). However, gyroscope mean offset in an axis can be as large as 0.02 rads^{-1}. The magnetometer provides data in μT, and magnetometer noise standard deviation was 0.95 μT. The manual does not specify magnetometer noise levels. Note, the manual caveats its accelerometer and gyroscope noise specifications (TDK 2017). The magnetometer was calibrated for hard and soft iron distortions by rotating the wavedrifter in all possible orientations. This calibration is repeated after wavedrifter deployments to reconfirm the calibration coefficients. The resulting vector magnetic field magnitude has only small (few percent) variations. The IMU data is converted to wavedrifter acceleration in earth coordinates (up, magnetic North, and magnetic East) using the MATLAB AHRS (Attitude, Heading, Reference System) library. The algorithm fuses acceleration, magnetometer, and gyroscope measurements to estimate orientation and its erros using a Kalman filter. Input parameters include the IMU noise parameters above. We analyze wavedrifter acceleration **a** in earth coordinates with components (a_x, a_y, a_z), where a_z is vertical acceleration (i.e. gravity is removed) and the horizontal acceleration component will be in the specified coordinate system. More information on the wavedrifter is provided in the Zenodo data repository (Feddersen et al. 2023), including a manual, CAD drawings,

Arduino code, MATLAB processing code, and sample data files.

3. Laboratory tests

3.1. Wavedrifter buoyancy and vertical oscillation mode

Because the wavedrifter is buoyant, any submergence or elevation will lead to vertical accelerations that will be damped by the drag of the wavedrifter. To investigate the mode of vertical oscillation, submergence tests were performed in a bucket filled with saltwater ($\rho \approx 1025$ kgm^{-3}). The bucket was filled to a depth of 10 cm. A wavedrifter was held fixed 6 cm below the surface such that the drifter was almost making contact with the bottom of the bucket. The wavedrifter was held still for 5 s and then released. The wavedrifters accelerated upwards, rose, breached the surface, and then oscillated vertically on the water surface with strong decay over a few seconds. After 3 s, waves that were generated by the breaching reflected off of the bucket sidewalls leading to further vertical oscillations. Thus, analysis was cutoff at 3 s. This test was performed a total of 3 times with two different wavedrifters. The vertical component of acceleration a_z was estimated as described in Section 2.4). Time is referenced to wavedrifter release time and the three tests were used to estimate wavedrifter-mean and standard deviation of $a_z(t)$.

The time evolution of the wavedrifter-mean vertical acceleration $a_z(t)$ is shown in Figure 2. The wavedrifter $a_z(t)$ were similar across tests as indicated by the small standard deviations. Right after release, the mean wavedrifter accelerates upwards due to buoyancy with maximum $a_z = 0.5$ ms^{-2}. Thereafter, the mean-wavedrifter decelerates (negative a_z) with minimum $a_z = -1.5$ ms^{-2} at $t = 0.64$ s associated with the wavedrifters partially-breaching the water surface.
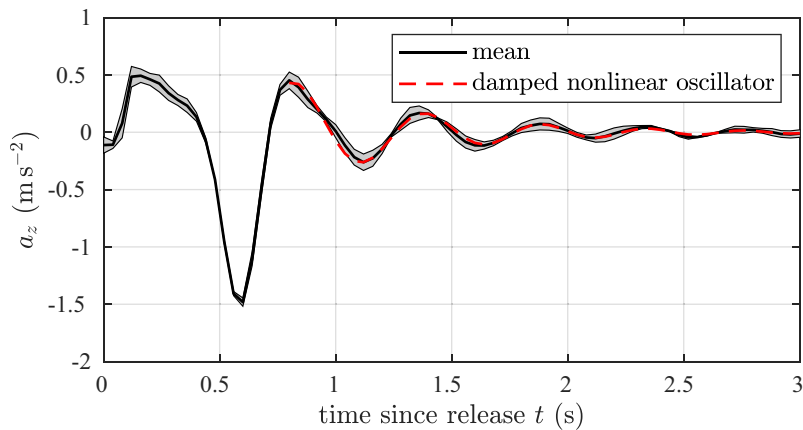
Figure 2. Wavedrifter-mean vertical acceleration a_z (black) with standard deviation (shading) versus time since release t for the buoyancy-induced vertical oscillation tests. The wavedrifter partially breaches with maximum position out of the water at $t = 0.6$ s with minimum $a_z \approx -1.5$ ms^{-2}. Note, the subsequent oscillation period shortens with time. The damped nonlinear oscillator model (1) versus time is shown as red-dashed.

The subsequent wavedrifter-mean maximum $a_z = 0.45$ ms^{-1} is associated with wavedrifter submergence. Thereafter, the mean wavedrifter accelerations become more time harmonic with a consistent decay rate that resembles a damped linear oscillator, but with an oscillation period that slowly decreases from 0.56 s between $t = 0.8$ and $t = 1.36$ s to a period of 0.38 s between $t = 2.36$ and $t = 2.74$ s. Period or frequency dependence on oscillation amplitude is consistent with forcing that is nonlinear with displacement (i.e. not Hooke's Law). For the fully submerged wavedrifter, only a water-based buoyancy force much smaller than gravity is felt. When fully emerged, the acceleration due to gravity is felt as air density is so low. For partial submergence, the buoyancy force is not linear with vertical position because the buoyancy is related to the submerged volume. Thus, subsequent to the second a_z maximum at $t = 0.8$ s, the evolution of the wavedrifter-mean acceleration closely resembles that of a damped nonlinear oscillator with

$$a_z = a_{z,0} \exp(-(t - t_0)/\tau) \cos\left(\omega_0(t - t_0) + \gamma(t - t_0)^2\right),$$
(1)

where $t_0 = 0.8$ s is the location of the acceleration peak (Figure 2), and the fit-parameters are $a_{z,0} = 0.45$ ms^{-2}, $\tau = 0.6$ s, $\omega_0 = 9.20$ rads^{-1} and $\gamma = 1.35$ rads^{-2}. It is useful to note that for a period of 0.6 s (or $2\pi/0.6$ rads^{-1}), an acceleration magnitude of 0.25 ms^{-2} implies a vertical oscillation amplitude of ± 2.3 mm. Thus, after the initial breach and submergence, the wavedrifter vertical position oscillations are relatively small. When deployed, the wavedrifter will be accelerated vertically by the wave field that is present which will induce small wavedrifter submergences when the sea surface accelerates rapidly. Thus, acceleration variability in a range of frequencies near 2 Hz is expected that should be treated as noise and not as surface gravity waves.

3.2. Wave channel tests

We next performed experiments at the glass channel at Scripps Institution of Oceanography's (SIO) Hydraulics Laboratory. The glass channel is a long channel with a piston wavemaker. The water depth was $h = 0.38$ m. Repeated packets of 30 waves at a frequency of $f = 1.5$ Hz (corresponding to $kh = 3.4$) were generated by the wavemaker. Each packet lasted 20 s and was repeated 9 times. Wave amplitude, measured by ruler, was $a \approx 0.013$ m resulting in a moderate $ak = 0.14$. A wavedrifter sampled the waves in the glass channel over these packets. wavedrifter vertical acceleration a_z time series show a series of nearly regular sinusoidal oscillations with amplitude 1.1 ms^{-2} (Figure 3a). The horizontal accelerations have
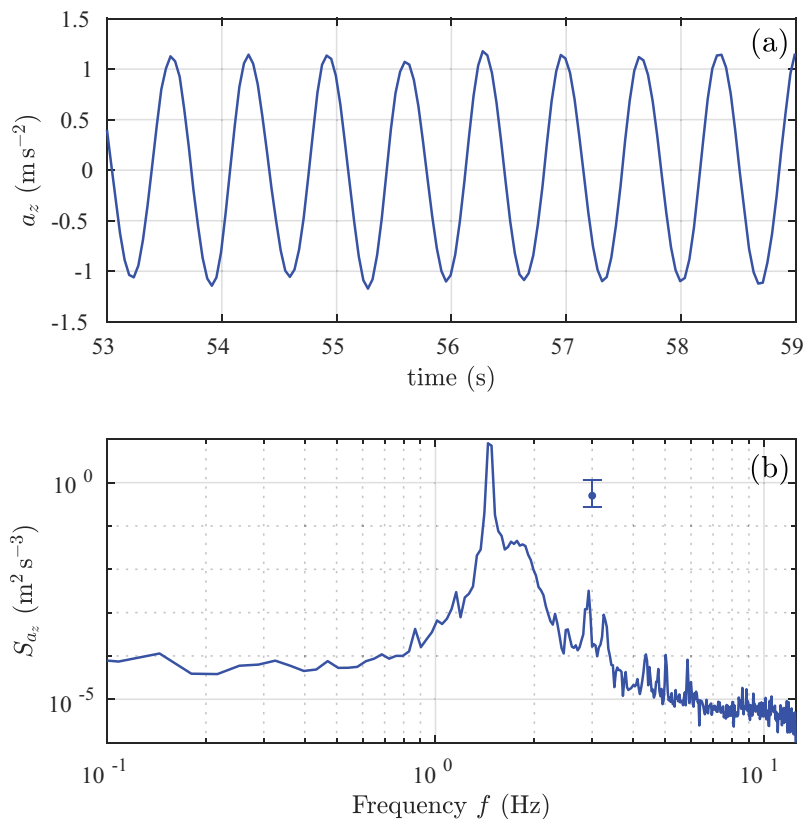
Figure 3. (a) Time series of wavedrifter vertical acceleration a_z over 6 seconds in the SIO Hydraulics Lab glass channel for monochromatic waves with frequency $f = 1.5$ Hz. (b) Vertical acceleration spectra S_{a_z} versus f from 180 s of data with 15 degrees-of-freedom and frequency resolution of 0.036 Hz. The error bar shows the 95% confidence limits.

very similar patterns just out of phase with a_z. For low-sloped waves (i.e. small ak), orbital excursions are small relative to the wavelength, and in such situations, via the surface kinematic boundary condition, the water surface elevation η is related to a_z via

$$\frac{\partial^2 \eta}{\partial t^2} = a_z. \qquad (2)$$

Using the frequency of 1.5 Hz, the a_z oscillations (Figure 3a) correspond to a wave amplitude of 0.012 m, consistent with ruler-based measurements.

We then examine the vertical acceleration spectra, S_{a_z}. As expected from the nearly sinusoidal time-series (Figure 3a), S_{a_z} has a strong peak at $f = 1.5$ Hz with a 0.05 Hz bandwidth related to the packet structure generated by the wavemaker (Figure 3b). At $f = 3$ Hz, a weak harmonic is present and at $f > 6$ Hz, a noise floor as been reached at $S_{a_z} < 10^{-5} \text{m}^2 \text{s}^{-3}$. This is consistent with the estimated spectral noise levels of $2 \times 10^{-6} \text{m}^2 \text{s}^{-3}$ as well as manual specified noise levels (Section 2.4). In the 0.5 Hz wide-band from 1.6 to 2 Hz, there are arguably elevated spectral levels near $S_{a_z} \approx 0.0035 \text{m}^2 \text{s}^{-3}$ (Figure 3b). A 0.4 Hz-wide flat spectrum at this level corresponds to a vertical acceleration standard deviation of 0.14 m s^{-2}, roughly consistent with the buoyancy-induced vertical oscillation mode (Figure 2). Thus, this likely represents the buoyancy-driven vertical oscillation mode and provides context for its potential spectral levels. Regardless, it is clearly much smaller than the overall wave signal.

Low-sloped (small ak) surface gravity waves, the ratio of horizontal to vertical velocity variance is related to $\tanh^2(kh)$ as are the particle accelerations (for small ak). We convert the horizontal acceleration spectra to vertical spectra and integrate over the $0.1 < f < 3$ Hz band. The standard deviation of converted horizontal accelerations is 0.78 ms^{-2} and that of vertical accelerations is 0.77 ms^{-2} with nearly identical spectra near the wave peak. This demonstrates that the wavedrifter is essentially water-following (or quasi-Lagrangian) for these laboratory conditions. Note, solutions to the Maxey-Riley equations (Maxey and Riley 1983), show that inertial particles increase their water following properties for fluid oscillations at longer time-scales and for stronger fluid velocities. Because, these wave velocities herein were very weak and at high frequency, we expect the wavedrifter to be water-following in ocean wave conditions.

4. Measuring wave overturning at the Surf Ranch

We now demonstrate how the wavedrifter can be used to measure strongly overturning waves and the subsequent transition to turbulence. Multiple wavedrifters were deployed over multiple waves at the Surf Ranch

wave basin, located in Lemoore, CA, USA on May 3 2022. Here, we report on a single drifter for a single wave to demonstrate the wavedrifter's capability as an instrument. Future work will use the wavedrifter data over multiple waves to characterize strongly overturning waves and the subsequently generated vortex and turbulence. The Surf Ranch generates an approximate soliton wave of ≈ 2 m height with a submerged hydrofoil towed along-basin on a tram. The along-basin hydrofoil speed is approximately $\approx 7.4 \text{ms}^{-1}$. The wave propagates up the slope and overturns on the barred-bathymetry designed to allow surfers the opportunity to get "tubed" (Figure 4). The Surf Ranch as a laboratory is detailed in Feddersen et al. (2023). Wavedrifters were released by swimmers so that they would be entrained by the wave overturn. As an example, a wavedrifter is seen in Figure 4 on the steep mid-face region of a wave that is overturning. This wavedrifter continues elevating up the wave-face to the roof of the overturn and is subsequently pitched forward and falls down with the overturn. Wavedrifter data was converted to earth coordinate accelerations as described in Section 2.4 where $+x$ acceleration is in the direction of wave propagation ($36°$ west of the along Surf Ranch direction), $+y$ acceleration is along the wave face, and $+z$ acceleration is upward.

We describe the method we used to systematically release wavedrifters at the same location with specific spacing. A float was anchored at a location prior to (offshore of) wave overturning, and a polypropylene (floating) line with 1-m separation distance markers was attached to the float. Prior to wave arrival, three swimmers held five to six wavedrifters in place at the water surface at assigned distance markers from the line so that the relative initial separation of the wavedrifters was known. Swimmers released the wavedrifters just prior to wave arrival. Overhead video of wavedrifter releases was captured by a DJI Phantom 4 unmanned aircraft system (UAS) at 30 Hz. A swimmer with a GoPro camera sampling at 120 Hz was used to capture wavedrifter motions within this wave overturn. The UAS and GoPro videos were time aligned to UTC and thus can be synced with wavedrifter observations. Here, we focus on a single wave observed by UAS and a GoPro camera and analyze a single wavedrifter

Figure 4. Photo of an overturning wave at the Surf Ranch. A wavedrifter is visible in the face of the wave (highlighted by the dashed yellow circle) just prior to overturning. Other wavedrifters, released by the swimmers, are present but not clearly visible. Photo by Israel Alemu.
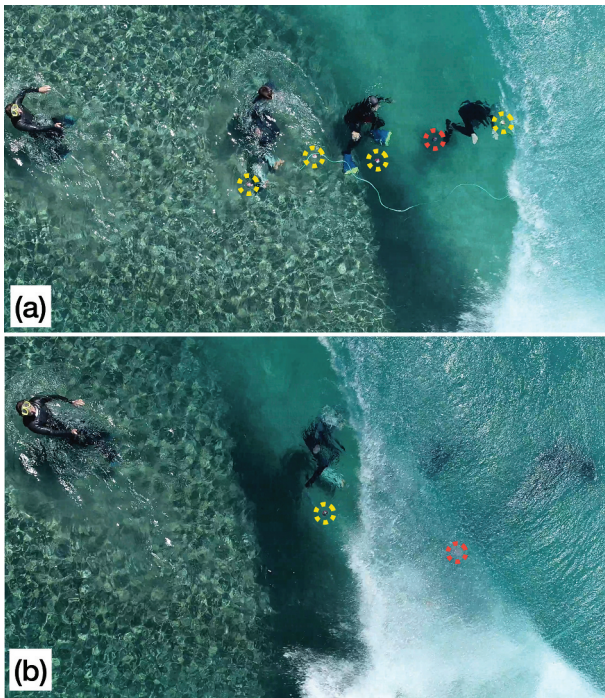
Figure 5. UAS-based photos looking down on the Surf Ranch overturning wave chosen for analysis. Visible wavedrifters are highlighted by a dashed circle, either red for the analyzed wavedrifter or yellow for other wavedrifters. Note the swimmer to the left taking GoPro video, the swimmers that released the wavedrifters, and the line used to align the releases. Time Δt is referenced to the moment that the entrained wavedrifter impacts the free surface. (a) At time $\Delta t = -0.729$ s, the wave is just starting to overturn at the location of the wavedrifters. Five wavedrifters are visible with the analyzed wavedrifter in second position. An additional wavedrifter is already obscured by the overturn. (b) At time $\Delta t = -0.396$ s, all but one wavedrifter has been obscured by the overturn. The analyzed wavedrifter is visible through the top transparent part of the overturn (red dashed circle) as the wavedrifter is being ejected forward with the overturning jet.

(marked by the red dashed circle in Figure 5 and red circle in Figure 6) to demonstrate its capability of measuring wave overturning and the subsequent turbulence after the overturn jet has impacted.

Time, denoted at Δt, is referenced to the moment that the wavedrifter, that is entrained in the overturning jet (or lip), impacts the wave surface in front. An example at time $\Delta t = -0.729$ s, is shown in Figure 5a, where an overturning wave is bearing down on the six just-released wavedrifters, of which five are visible. The analyzed wavedrifter (indicated with a red dashed circle in Figure 5) is on the lower part of the sloped wave-face. At a time $\Delta t = -0.396$ s,(or 0.333 s later), the wave has propagated forward such that only the last wavedrifter is visible on the water surface (yellow dashed circle in Figure 5b). However, the analyzed wavedrifter (marked in red dashed), can now be seen embedded within the top of the overturn (red dashed circle).

Swimmer-captured GoPro images are shown in Figure 6 and are used to contextualize the wavedrifter

observations. Quantitative comparison between video and wavedrifter is not possible as stereo-camera systems are required for quantitative reconstruction of wave surface (Bergamasco et al. 2017). At time $\Delta t = -0.603$ s, the wavedrifter is being lifted upward by the very steep wave-face (Figure 6a). This is 0.126 s after the time in Figure 5a when the wavedrifter was on the lower-sloped part of the wave. At time $\Delta t = -0.403$ s, the wavedrifter is on the roof of the overturn, and is being advected forward in the wave propagation direction $+x$ (Figure 6b). Concurrently, the wavedrifter is seen in the roof of the overturn in Figure 5b. At time $\Delta t = -0.203$ s, the wavedrifter is falling down with the overturning jet as it also moves farther forward of the propagating wave (Figure 6c). At time $\Delta t = -0.033$ s, the wavedrifter is about to hit the splash-up of the impacting jet (Figure 6d). In the next video frame, the wavedrifter is embedded in the splash-up and no longer visible.

We now examine the earth coordinate acceleration $\mathbf{a}(t) = (a_x(t), a_y(t), a_z(t))$ of the analyzed wavedrifter (Figure 7) where the vertical magenta lines represent the times of images in Figure 6. Recall that the wavedrifter IMU samples at 25 Hz corresponding to 40 ms sampling time. We focus first on the overturning stage $\Delta t < 0$ during which the along-wave accelerations a_y are small. At time $\Delta t < -1.4$ s, wavedrifter acceleration is near-zero in all 3 components. At $\Delta t \approx -1$ s, vertical acceleration begins increasing reaching a maximum of $a_z = 0.9g$ near $\Delta t = -0.6$ s (first magenta line in Figure 7a). This corresponds to the wavedrifter being mid-face on the nearly-vertically sloped wave face (Figure 6a). The horizontal wave-direction acceleration a_x begins increasing just after a_z does. A maximum of $a_x = 3.67g$ is reached at $\Delta t = -0.47$ s, at which point the wavedrifter is already accelerating downward ($a_z < 0$). At time $\Delta t = -0.403$ s (second magenta line in Figure 7), the wavedrifter is on the upper-back portion of the overturn (Figure 6b). At this time, the peak horizontal acceleration maximum has passed but $a_x \approx 1.2g$ is still substantial, and the downward acceleration has an extrema with $a_z = -3.2g$. The large a_x and a_z magnitudes during $-0.6 < \Delta t < -0.3$ s are likely due to the centripetal acceleration associated with the wavedrifter rapidly traversing the tight curve of the upper-back portion of the overturn, and are consistent with the large acceleration magnitudes in this region seen in smoothed particle hydrodynamics modeling of a wave overturn (Landrini et al. 2007). As the wavedrifter begins falling within the overturning jet, a_z begins asymptoting to $-g$ as the centrifugal forces decrease indicating free-fall and the $a_x \approx 0$. The image at $\Delta t = -0.203$ (Figure 6c; corresponding to the third magenta line in Figure 7) is consistent with the wavedrifter, embedded in the overturning

Figure 6. Sequential images of Surf Ranch wave overturning for the wave in Figure 5. The analyzed wavedrifter is circled in red at specific times before wavedrifter impact: (a) $\Delta t = -0.603$ s as the wavedrifter is advected upward on the near vertical wave face, (b) $\Delta t = -0.403$ s as the wavedrifter is on the roof of the wave overturn, (c) $\Delta t = -0.203$ s as the wavedrifter is falling with the lip, and (d) $\Delta t = -0.033$ s as the wavedrifter is about to impact the water below. Swimmers who released the wavedrifters are visible ducking under the overturning wave.

jet, largely being in free-fall with $a_z = -1.1g$ and $a_x = 0.1g$. At time $\Delta t = -0.033$ just before the wavedrifter makes contact with the splash up (Figure 6d), the wavedrifter is essentially in a complete free fall with $a_z = -1.05g$ and $a_x = 0.05g$. The evolution of a_x and a_z during the overturning stage is qualitatively
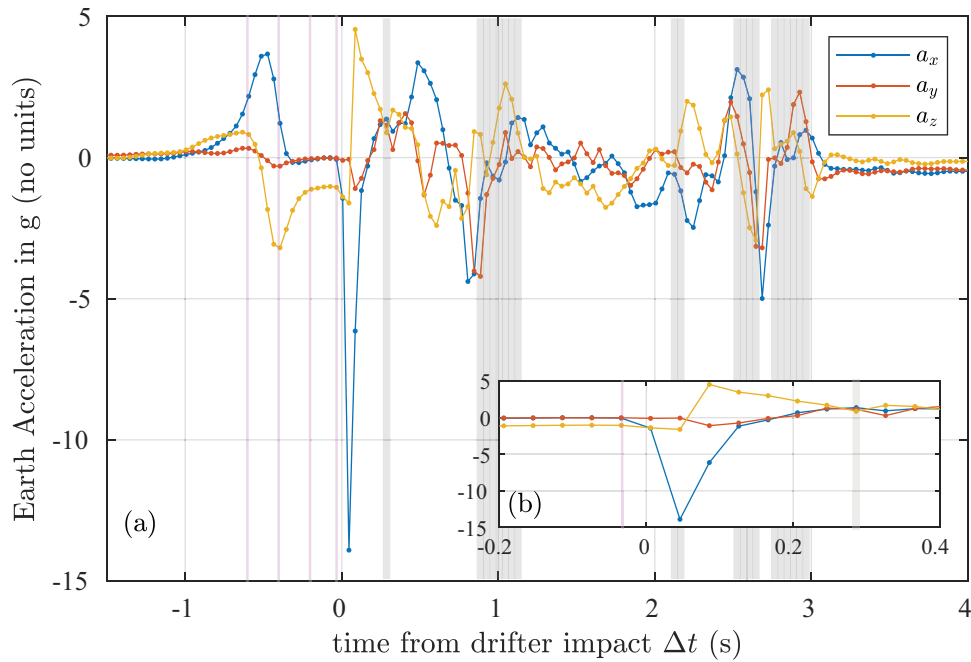
Figure 7. Wavedrifter acceleration normalized by gravity in earth coordinates versus time from wavedrifter impact Δt: Accelerations components are in the wave propagation direction a_x (blue), the along-wavecrest direction a_y (orange), and the vertical direction a_z (yellow). Each sample time is indicated with a dot. Vertical magenta lines represent the Δt of the four sequential images in Figure 6. Panel (a) shows 6 s of time and inset panel (b) shows the 0.6 s of times near wavedrifter impact at $\Delta t = 0$ s.

consistent with accelerations inferred from potential-flow boundary element method numerical simulations of a soliton overturning on a step reef (Yasuda, Mutsuda, and Mizutani 1997).

For $\Delta t > 0$ s, denoted the *turbulent-transition* stage, the wavedrifter embedded within the wave jet has impacted the water surface in front of the wave, there is substantial splash up, and the wavedrifter is no longer visible. Immediately, upon impact, the acceleration spikes to extrema of $a_x = -14g$ and $a_z = 4.5g$ (Figure 7b) and both a_x and a_z vary rapidly over the course of a few 40 ms samples. Because of the finite size and mass of the wavedrifter and likely the strong fluid gradients at impact, this impact wavedrifter acceleration may not match the largest fluid parcel accelerations. In addition, the wavedrifter's 25 Hz sampling rate may be not be fast enough to resolve the near-impact accelerations. Shortly thereafter by $\Delta t = 0.2$ s, the acceleration still varies substantially from $\pm 3g$ but not nearly as rapidly as upon impact. For $\Delta t > 1$ s, the y-acceleration a_y varies as much as the other components of acceleration indicating a transition to isotropic turbulence. At $\Delta t > 3.25$ s, the accelerations become weaker and more steady indicating that the wavedrifter is out of an active turbulence field and perhaps is embedded in the long-period seiche (with nonzero horizontal accelerations) induced by the breaking soliton.

Note, AHRS solutions when local accelerations are order of or stronger than gravity can be uncertain. Averaging over $-1.5 < t < 4$ s results in a mean vertical acceleration of $0.1g$, small relative to the overall magnitude of accelerations, suggesting that the AHRS solution is reasonable. Another concern is that the large wavedrifter angular velocities could lead to the IMU reading large accelerations due to the IMU not being aligned with the rotational center of mass. The external housing has the majority of the mass and contributes the most to the rotational center of mass, thus we assume the center of volume is the rotational center of mass. The accelerometer is located within $r = 0.5$ cm (on two axes) and $r = 1$ cm (on another axis) of the wavedrifter center of volume. Thus, a spin rate (angular velocity) of $\dot{\theta} = 600$ dps, would induce an apparent acceleration magnitude of $r\dot{\theta}^2$ that is 6% or 12% of gravity and is thus small relative to the observed earth coordinate accelerations. During the overturning stage ($\Delta t < 0$) the spin rate is nearly always small. We highlight the times when any component of angular velocity magnitude is > 600 dps with vertical gray bars in Figure 7. In the overturning phase ($\Delta t < 0$ s), at no time was angular velocity elevated, indicating that the estimated **a** are not contaminated by centrifugal accelerations. During the turbulent-transition stage ($\Delta t > 0$), elevated angular velocities occur 20% of the time mostly in two groups, one near $\Delta t = 1$ s and another at $2.5 < \Delta t < 3$ s. At no time did any component of angular velocity exceed 1000 dps (recall the maximum range is 2000 dps), implying at most $0.15-0.3g$, which is still far smaller than the observed **a** variability during the *turbulent-transition* stage. This suggests that the

IMU accelerometer is not contaminated by centrifugal acceleration induced noise and that the wavedrifter can effectively sample the turbulent field within an actively breaking wave.

We explore further the wavedrifter capability by examining the particle trajectories implied by the earth coordinate accelerations. We define the wavedrifter position vector $\mathbf{x}(t) = (x, y, z)$. We integrate the acceleration vector $\mathbf{a}$ twice,

$$\mathbf{x}(\Delta t) = \int_{\Delta t_0}^{\Delta t} \int_{\Delta t_0}^{t'} \mathbf{a}(\tilde{t}) d\tilde{t} dt' \tag{3}$$

where $\Delta t_0 = -1.5s$ and assuming zero initial velocity and an initial position of $\mathbf{x} = (0, 0, 0)$ m. The integration is done simply using the trapezoid rule and does not use more complex acceleration integration algorithms of control theory. Because a_y is weak during the overturning phase, we show the evolution of $\mathbf{x}$ in the (x, z) plane over $\Delta t \in (-1.5, 1.2)$ s in Figure 8a. We limit the time-duration of the integration as long-integrations of acceleration are well understood to lead to significant drift.

We first explore the inferred wavedrifter trajectories in the fixed (x, z) reference frame. Initially, the wavedrifter is at $(x, z) = (0, 0)$ m, with a subsequent slight $-x$ motion that leads to the wavedrifter rising such that at $\Delta t = -0.603$ (Figure 6a), the wavedrifter is 0.6 m above the initial location. The wavedrifter continues rising but is moved forward ($+x$) more rapidly. Near $\Delta t = -0.403$ s (Figure 6b), the wavedrifter reaches a maximum z of 1.3 m and is moved forward rapidly. At $\Delta t = -0.203$ s (Figure 6c), the wavedrifter has just started falling and follows a relatively straight trajectory until $\Delta t = -0.033$ s (Figure 6d, when the

wavedrifter is last visible) where the wavedrifter has moved 4 m forward and is at $z = 0.5$ m just before it impacts the splash up. In the turbulent-transition stage ($\Delta t > 0$ s), the wavedrifter is at first driven down to $z = -0.6$ m, looping backward slightly. It then moves forward again in an arc to near $z = 0$ m before being driven downward again to $z = -0.71$ m at $\Delta t = 1.11$ s. This is indicative of the wavedrifter being advected by a coherent vortex induced by the broken wave overturn.

We next examine the wavedrifter trajectories in a reference frame moving with wave (x', z) where $x' = x - C\Delta t$ where the wave speed $C \approx 6$ ms^{-1} is estimated from the along-basin foil speed (≈ 7.4 ms^{-1}) and the 36° wave propagation direction and x' is offset so that so the maximum z is located at $x' = 0$ (Figure 8b). We first examine the overturning stage. Initially, the wavedrifter is far ahead of the wave at $z = 0$ m and is moving backwards "toward" the wave. Near $x' = 1$ m, the wavedrifter starts rising and at $x = -0.25$ m, makes a rapid turn shooting forward first, upward briefly and then downward. The locations of the magenta symbols in Figure 8b are consistent with the wavedrifter locations in Figure 6. Overall, the wavedrifter trajectories in this stage strongly resemble the classic shape of wave overturning (e.g. Blenkinsopp and Chaplin 2008; Feddersen et al. 2023; Longuet-Higgins 1982; O'Dea, Brodie, and Elgar 2021), suggesting wavedrifter positions are accurate. Note that the wavedrifter trajectory is Lagrangian and should not be interpreted as the overturn shape at a fixed time. In the turbulent-transition stage ($\Delta t > 0$ s), the wavedrifter is driven downward and left behind the wave moving in $-x'$. At about $x' = -1.5$ m, the
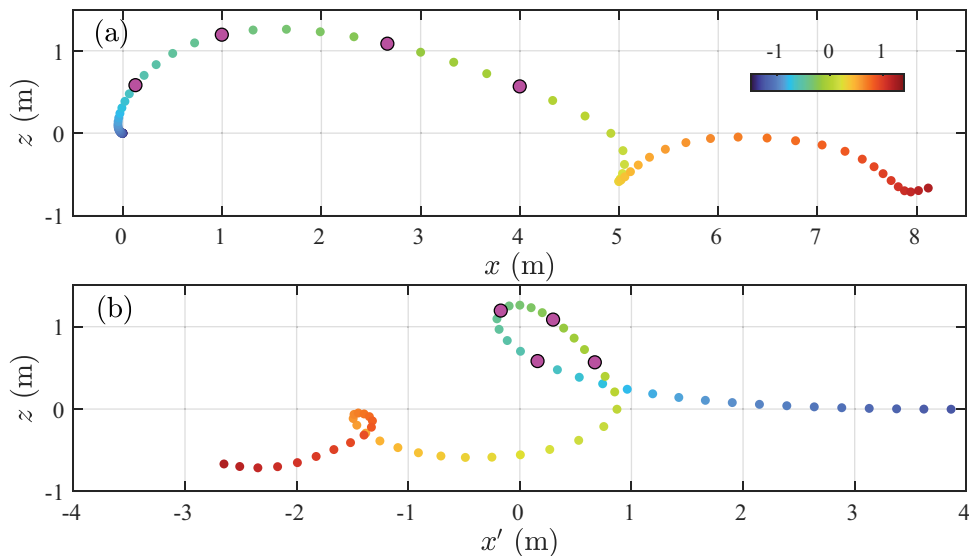
Figure 8. Wavedrifter position evolution with time (colored) in (a) fixed (x, z) coordinates and (b) coordinates moving in the wave reference frame (x', z) where $x' = x - C\Delta t$, where $C \approx 6$ms^{-1} is the speed in the direction of wave propagation. In both, the colors represent time Δt and a point is shown every 40 ms (25 Hz). Separation between the points gives a sense of velocity. The times of the 4-images in Figure 6 are indicated as magenta circles. Positions are derived by integrating twice the earth coordinate accelerations (Figure 7) using (3).

wavedrifter is raised up and loops tightly back downward continuing to move in $-x$, again consistent with a coherent vortex. Future research will use multiple wavedrifters over multiple waves to examine the detailed kinematics of wave overturning, the evolution of the vortical features generated via wave overturning, and how the post-breaking acceleration measurements can be used to estimate energy dissipation rates.

5. Limitations and improvements

A significant limitation to using the wavedrifter in field settings is the issue of locating and recovering the wavedrifter. Due to size, battery power, and cost constraints, the wavedrifter lacks telemetry – a feature of most GPS and IMU wave buoys (e.g. Rabault et al. 2022; Raghukumar et al. 2019). A wavedrifter released in field-scale overturning waves is easily lost. One possibility is to fasten a leash on the wavedrifter using very thin yet strong fishing line attached to a swimmer or to a larger and far more visible float allowing the wavedrifter to be recovered. With a leash, care must be taken that there is sufficient slack and scope so that the wavedrifter is water-following (Lagrangian) and not contaminated by forces imparted by the leash. Additional concerns include potentially having the leash foul on any surfers, swimmers, or watercraft in the region. Another possibility is to place a small active RFID tag into the wavedrifter. Such a tag would broadcast wavedrifter position so that a recovery team within ≈ 50 m would be able to locate and recover the wavedrifter. This would allow field-released wavedrifters to be found in regions where wavedrifters are likely beaching themselves or accumulating in a lagoon. Reflective solas tape or day glo paint may also help in being able to locate wavedrifters. Wavedrifters ejecting offshore in a rip current are, however, unlikely to be found.

The wavedrifter could be improved in other ways. First, the GPS is used here simply to get a UTC time reference to align with video of the wavedrifter. This GPS does not provide number of satellites, nor does it provide HDOP; thus, solution quality is unknown. The GPS also does not provide a vertical location which would be useful in constraining position integrations (3). The GPS latitude and longitude are intermittent and drift when lock is reacquired. The Adafruit Mini GPS PA1010D used here is inexpensive with easy Arduino integration but another GPS solution would improve the wavedrifter dramatically. Faster IMU sampling perhaps would allow the accelerations right at overturning jet impact to be resolved. Increasing battery capacity beyond the current 1 h would enable new missions. Further improvements could include further miniaturization by fabricating a custom board holding all the electronics and processors, making the drifter even more water following. Improving power consumption can also improve deployment times. For some applications, a specific gravity closer to but still less than one (rather than 0.84) may be desirable.

6. Discussion and a future experiment

Low-cost, small, water following, IMU-based wavedrifters are a useful tool for probing aspects of nonlinear surface gravity wave steepening and overturning kinematics and the subsequent transition to turbulence in both shallow and deep water. Wavedrifter buoyancy response was detailed with laboratory experiments. Wavedrifters accurately measure small high-frequency waves in a laboratory wave flume and were demonstrated to be water following, that is Lagrangian. We highlight a potential field-scale application where the wavedrifter can be used to measure the Lagrangian accelerations in steepening and overturning of highly nonlinear surface gravity waves as well as the transition to turbulence during wave breaking. The small size (5 cm sphere), high-drag, and low mass (77 g) of the wavedrifter enables these kinds of measurements. This contrasts with the non-water following 40 cm diameter and 1 kg IMU wave buoy used to identify surfzone wave breaking events (Brown and Paasch 2021) analogous to deep water methods (Brown et al. 2018).

We close with proposing a future field experiment. Since the work of Duncan (1981), it is well understood that wave breaking imparts a force onto the water surface, essentially transferring momentum. Numerical (Deike, Pizzo, and Melville 2017) and laboratory (Lenain, Pizzo, and Melville 2019) experiments have clearly shown how the breaking of a single focused deep water wave packet induces flow accelerations. A swarm deployment of wavedrifters (given the limitations discussed above) in a deep-water whitecapping wave field would measure both the occurrence of wave breaking but also the accelerations and drift induced by it. Deployments across wave ages could quantify the bulk effect of wave breaking on air-sea momentum transfer. Such observations can then be linked to statistical models for bulk air-sea fluxes (e.g. Romero 2019) or whitecap coverage (e.g. Brumer et al. 2017).

Disclosure statement

Funding

ORCID

F. Feddersen http://orcid.org/0000-0002-5488-9074

References

Amador, A., and M. Canals. 2016. "Design and Development of an Instrumented Drifter for Lagrangian Measurements of Inertial Particle Dynamics in Breaking Waves." *IEEE Journal of Oceanic Engineering* 41 (1): 82–93. https://doi.org/10.1109/JOE.2015.2389591.

Amador, A., M. Canals, G., Guerrero, J. Cruz, and E. Ortiz. 2012. "Development of Novel Instrumented Lagrangian Drifters to Probe the Internal Structure of Breaking Surface Waves." In *2012 Oceans*, Hampton Roads VA USA, 1–6. IEEE. https://doi.org/10.1109/OCEANS.2012.6404992.

Amador, A., S. T. Merrifield, and E. J. Terrill. 2023. "Assessment of Atmospheric and Oceanographic Measurements from an Autonomous Surface Vehicle." *Journal of Atmospheric and Oceanic Technology* 40 (3): 305–326. https://doi.org/10.1175/JTECH-D-22-0060.1 .

Bergamasco, F., A. Torsello, M., Sclavo, F. Barbariol, and A. Benetazzo. 2017. "WASS: An Open-Source Pipeline for 3D Stereo Reconstruction of Ocean Waves." *Computers & Geosciences* 107:28–36. https://doi.org/10.1016/j.cageo.2017.07.001.

Blenkinsopp, C. E., and J. R. Chaplin. 2008. "The Effect of Relative Crest Submergence on Wave Breaking Over Submerged Slopes." *Coastal Engineering* 55 (12): 967–974. https://doi.org/10.1016/j.coastaleng.2008.03.004.

Brown, A. C., and R. K Paasch. 2021. "The Accelerations of a Wave Measurement Buoy Impacted by Breaking Waves in the Surf Zone." *Journal of Marine Science and Engineering* 9 (2): 214. https://doi.org/10.3390/jmse9020214.

Brown, A., J. Thomson, A. Ellenson, H Tuba Özkan-Haller Fadia Ticona Rollano, and M. C. Haller. 2018. "Kinematics and Statistics of Breaking Waves Observed Using SWIFT Buoys." *IEEE Journal of Oceanic Engineering* 44 (4): 1011–1023. https://doi.org/10.1109/JOE.2018.2868335.

Brumer, S. E., C. J. Zappa, I. M. Brooks, H. Tamura, S. M. Brown, B.W. Blomquist, C.W. Fairall, and A. Cifuentes-Lorenzen. 2017. "Whitecap Coverage Dependence on Wind and Wave Statistics as Observed During so GasEx and HiWings." *Journal of Physical Oceanography* 47 (9): 2211–2235. https://doi.org/10.1175/JPO-D-17-0005.1.

Bullock, G. N., C. Obhrai, D. H. Peregrine, and H. Bredmose. 2007. "Violent Breaking Wave Impacts. Part 1: Results from Large-Scale Regular Wave Tests on Vertical and Sloping Walls." *Coastal Engineering* 54 (8): 602–617. https://doi.org/10.1016/j.coastaleng.2006.12.002.

Carini, R. J., C. Chris Chickadel, A. T. Jessup, and J. Thomson. 2015. "Estimating Wave Energy Dissipation in the Surf Zone Using Thermal Infrared Imagery." *Journal of Geophysical Research: Oceans* 120 (6): 3937–3957. https://doi.org/10.1002/2014JC010561.

Centurioni, L., L. Braasch, E. Di Lauro, P. Contestabile, F. De Leo, R. Casotti, L. Franco, and D. Vicinanza. 2017. "A New Strategic Wave Measurement Station off Naples Port Main Breakwater." *Coastal Engineering Proceedings* 1 (35): 36. https://doi.org/10.9753/icce.v35.waves.36.

Centurioni, L. R., J. Turton, R. Lumpkin, L. Braasch, G. Brassington, Y. Chao, E. Charpentier, et al. 2019. "Global in situ Observations of Essential Climate and Ocean Variables at the Air–Sea Interface." *Frontiers in Marine Science* 6:419. https://doi.org/10.3389/fmars.2019.00419.

Collins, Clarence O., Patrick Dickhudt, Jim Thomson, Eric Terrill, and Luca Centurioni. 2023. "Performance of Moored GPS Wave Buoys." *Coastal Engineering Journal*.

Deike, Luc. 2022. "Mass Transfer at the Ocean–Atmosphere Interface: The Role of Wave Breaking, Droplets, and Bubbles." *Annual Review of Fluid Mechanics* 54 (1): 191–224. https://doi.org/10.1146/annurev-fluid-030121-014132.

Deike, Luc, Nick Pizzo, and W. K. Melville. 2017. "Lagrangian Transport by Breaking Surface Waves." *Journal of Fluid Mechanics* 829:364–391. https://doi.org/10.1017/jfm.2017.548.

Derakhti, M., J. T Kirby, M. L Banner, S. T Grilli, and J. Thomson. 2020. "A Unified Breaking Onset Criterion for Surface Gravity Water Waves in Arbitrary Depth." *Journal of Geophysical Research: Oceans* 125 (7): e2019JC015886. https://doi.org/10.1029/2019JC015886.

Duncan, J. H. 1981. "An Experimental Investigation of Breaking Waves Produced by a Towed Hydrofoil." *Proceedings of the Royal Society of London: A Mathematical and Physical Sciences* 377 (1770): 331–348.

Feddersen, Falk. 2012. "Scaling Surf Zone Turbulence." *Geophysical Research Letters* 39 (18): n/a–n/a. L18613. https://doi.org/10.1029/2012GL052970.

Feddersen, F., A. Amador, K., Pick, A., Vizuet, K., Quinn, E Wolfinger, J. H. MacMahan, and A. Fincham. 2023. *Wavedrifter: Manual, CAD Files, Arduino Code, MATLAB Processing Code, and Sample Code from Surf Ranch*. Zenodo.org. https://doi.org/10.5281/zenodo.8000280.

Feddersen, F., A. M. Fincham, K. L. Brodie, A. D. Young, M. S. Spydell, D. J. Grimes, M. Pieska, and K. Hanson. 2023. "Cross-Shore Wind-Induced Changes to Field-Scale Overturning Wave Shape." *Journal of Fluid Mechanics* 958. https://doi.org/10.1017/jfm.2023.40.

Feddersen, F., R. T. Guza, S. Elgar, and T. H. C. Herbers. 1998. "Alongshore Momentum Balances in the Nearshore."

Journal of Geophysical Research: Oceans 103 (15): 15667–15676. https://doi.org/10.1029/98JC01270.

Fiedler, J. W., L. Kim, R. L. Grenzeback, A. P Young, and M. A Merrifield. 2021. "Enhanced Surf Zone and Wave Runup Observations with Hovering Drone-Mounted Lidar." *Journal of Atmospheric and Oceanic Technology* 38 (11): 1967–1978.

Govender, K., R. Mukaro, and G. Mocke. 2023. "Laboratory Measurements of Mean and Turbulence Velocities and Shear Stresses Through the Wave Roller in Strong Plunging Waves." *Coastal Engineering* 180:104254. https://doi.org/10.1016/j.coastaleng.2022.104254 .

Haines, John W, and Asbury H Sallenger. 1994. "Vertical Structure of Mean Cross-Shore Currents Across a Barred Surf Zone." *Journal of Geophysical Research: Oceans* 99 (C7): 14223–14242. https://doi.org/10.1029/94JC00427 .

Herbers, T. H. C., P. F. Jessen, T. T. Janssen, D. B. Colbert, and J. H. MacMahan. 2012. "Observing Ocean Surface Waves with GPS-Tracked Buoys." *Journal of Atmospheric and Oceanic Technology* 29 (7): 944–959. https://doi.org/10.1175/JTECH-D-11-00128.1.

Hoefel, F., and S. Elgar. 2003. "Wave-Induced Sediment Transport and Sandbar Migration." *Science: Advanced Materials and Devices* 299 (5614): 1885–1887. https://doi.org/10.1126/science.1081448.

Holman, R., and Merrick C. Haller. 2013. "Remote Sensing of the Nearshore." *Annual Review of Marine Science* 5 (1): 95–113. PMID: 22809186. https://doi.org/10.1146/annurev-marine-121211-172408 .

Jessup, A. T., C. J. Zappa, M. R. Loewen, and V. Hesany. 1997. "Infrared Remote Sensing of Breaking Waves." *Nature* 385 (6611): 52–55. https://doi.org/10.1038/385052a0.

Kodaira, T., T. Katsuno, Y., Fujiwara, T Nose, J., Rabault, J., Voermans, M., Kimizuka, J., Inoue, T. Toyota, and T. Waseda. 2022. "Development of MEMS IMU Based and Solar Powered Wave Buoy FZ." In *OCEANS 2022*, Hampton Roads, 1–6. IEEE. https://doi.org/10.1109/OCEANS47191.2022.9977128.

Kohout, A. L., B. Penrose, S., Penrose, and M. JM Williams. 2015. "A Device for Measuring Wave-Induced Motion of Ice Floes in the Antarctic Marginal Ice Zone." *Annals of Glaciology* 56 (69): 415–424. https://doi.org/10.3189/2015AoG69A600.

Landrini, M., M. Greco A Colagrossi, M. P. Tulin, and M. P. TULIN. 2007. "Gridless Simulations of Splashing Processes and Near-Shore Bore Propagation." *Journal of Fluid Mechanics* 591 (June 2003): 183–213. https://doi.org/10.1017/S0022112007008142 .

Lenain, L., and N. Pizzo. 2020. "The Contribution of High-Frequency Wind-Generated Surface Waves to the Stokes Drift." *Journal of Physical Oceanography* 50 (12): 3455–3465. https://doi.org/10.1175/JPO-D-20-0116.1.

Lenain, Luc, Nick Pizzo, and W. K. Melville. 2019. "Laboratory Studies of Lagrangian Transport by Breaking Surface Waves." *Journal of Fluid Mechanics* 876:R1. https://doi.org/10.1017/jfm.2019.544.

Longuet-Higgins, M. S. 1982. "Parametric Solutions for Breaking Waves." *Journal of Fluid Mechanics* 121 (–1): 403–424. https://doi.org/10.1017/S0022112082001967.

Longuet-Higgins, M. S., D. E. Cartwright, and N. D. Smith. 1963. Ocean Wave Spectra, *Chap. Observations of the Directional Spectrum of Sea Waves Using the Motions of a Floating Buoy*, 111–136. Upper Saddle River, NJ, USA: Prentice Hall.

Maxey, Martin R., and James J. Riley. 1983. "Equation of Motion for a Small Rigid Sphere in a Nonuniform Flow." *The Physics of Fluids* 26 (4): 883–889. https://doi.org/10.1063/1.864230.

Mitsuyasu, Hisashi, Fukuzo Tasai, Toshiko Suhara, Shinjiro Mizuno, Makoto Ohkusu, Tadao Honda, and Kunio Rikiishi. 1975. "Observations of the Directional Spectrum of Ocean WavesUsing a Cloverleaf Buoy." *Journal of Physical Oceanography* 5 (4): 750–760. https://doi.org/10.1175/1520-0485(1975)005<0750:OOTDSO>2.0.CO;2.

Mostert, W., S. Popinet, and L. Deike. 2022. "High-Resolution Direct Simulation of Deep Water Breaking Waves: Transition to Turbulence, Bubbles and Droplets Production." *Journal of Fluid Mechanics* 942:A27. https://doi.org/10.1017/jfm.2022.330.

Nose, T., T. Katsunoa, T., Wasedaa, Shuki Ushiob C., J., Rabaultd, T., Kodairaa, and J. Voermans. 2023. "Observation of Wave Propagation Over 1,000 Km into Antarctica Winter Pack Ice." *Coastal Engineering Journal*.

O'Dea, A., K. Brodie, and S. Elgar. 2021. "Field Observations of the Evolution of Plunging-Wave Shapes." *Geophysical Research Letters* 48 (16): e2021GL093664. https://doi.org/10.1029/2021GL093664.

Rabault, J., T. Nose, G., Hope, M., Müller, Ø., Breivik, J. Voermans, L., Robert Hole, et al. 2022. "Openmetbuoy-v2021: An Easy-To-Build, Affordable, Customizable, Open-Source Instrument for Oceanographic Measurements of Drift and Waves in Sea Ice and the Open Ocean." *Geosciences* 12 (3): 110. https://doi.org/10.3390/geosciences12030110.

Rabault, J., G., Sutherland, B., Ward, K. H., Christensen, T., Halsne, and A Jensen. 2016. "Measurements of Waves in Landfast Ice Using Inertial Motion Units." *IEEE Transactions on Geoscience and Remote Sensing* 54 (11): 6399–6408. https://doi.org/10.1109/TGRS.2016.2584182.

Raghukumar, K., G. Chang, F., Spada, C., Jones, T., Janssen, and A. Gans. 2019. "Performance Characteristics of "Spotter," a Newly Developed Real-Time Wave Measurement Buoy." *Journal of Atmospheric and Oceanic Technology* 36 (6): 1127–1141. https://doi.org/10.1175/JTECH-D-18-0151.1.

Rainville, E. J., J. Thomson, M. Moulton, and M. Derakhti. 2023. "Measurements of Nearshore Waves Through Coherent Arrays of Free-Drifting Wave Buoys." *Earth System Science Data Discussions* 2023:1–22. https://doi.org/10.5194/essd-2023-64.

Romero, Leonel. 2019. "Distribution of Surface Wave Breaking Fronts." *Geophysical Research Letters* 46 (17–18): 10463–10474. https://doi.org/10.1029/2019GL083408.

Saez, Francisco J, Patricio A Catalan, and Carlos Valle. 2021. "Wave-By-Wave Nearshore Wave Breaking Identification Using U-Net." *Coastal Engineering* 170:104021. https://doi.org/10.1016/j.coastaleng.2021.104021.

Smit, P. B., I. A. Houghton, K. Jordanova, T. Portwood, E. Shapiro, D. Clark, M. Sosa, and T. T. Janssen. 2021. "Assimilation of Significant Wave Height from Distributed Ocean Wave Sensors." *Ocean Modelling* 159:101738. https://doi.org/10.1016/j.ocemod.2020.101738.

TDK. 2017. *TDK Invensense ICM-20948*. https://invensense.tdk.com/wp-content/uploads/2016/06/DS-000189-ICM-20948-v1.3.pdf.

Thomson, Jim. 2012. "Wave Breaking Dissipation Observed with "SWIFT" Drifters." *Journal of Atmospheric and Oceanic*

Technology 29 (12): 1866–1882. https://doi.org/10.1175/JTECH-D-12-00018.1.

Thomson, J., P. Bush, V., Castillo, N. Clemetta Jacob Davis, A., de Klerk, E., Iseley, E. J. Rainville, B. Salmi, J. Talbert, and M. Moulton. 2023. "Development and Testing of microSwift Expendable Wave Buoys." *Coastal Engineering Journal.*

Thomson, J., M. Moulton, A., de Klerk, J., Talbert, M., Guerra, S., Kastner, M., Smith, M. Schwendeman, S., Zippel, and S. Nylund. 2019. "A New Version of the SWIFT Platform for Waves, Currents, and Turbulence in the Ocean Surface Layer." In *2019 IEEE/OES Twelfth Current, Waves and Turbulence Measurement (CWTM)*, San Diego, 1–7. https://doi.org/10.1109/CWTM43797.2019.8955299. IEEE.

Vittori, G. 2003. "Sediment Suspension Due to Waves." *Journal of Geophysical Research: Oceans* 108 (C6). https://doi.org/10.1029/2002JC001378.

Yasuda, T., H., Mutsuda, and N. Mizutani. 1997. "Kinematics of Overturning Solitary Waves and Their Relations to Breaker Types." *Coastal Engineering* 29 (3): 317–346. https://doi.org/10.1016/S0378-3839(96)00032-4.